Accepted Manuscript

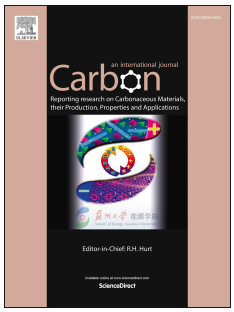

Hydrogen-bond supramolecular hydrogels as efficient precursors in the preparation of freestanding 3D carbonaceous architectures containing BCNO nanocrystals and exhibiting a high CO_2/CH_4 adsorption ratio

N. López-Salas, M.L. Ferrer, M.C. Gutiérrez, J.L.G. Fierro, C. Cuadrado-Collados, J. Gandara-Loe, J. Silvestre-Albero, F. del Monte

PII: S0008-6223(18)30318-X

DOI: 10.1016/j.carbon.2018.03.066

Reference: CARBON 13009

To appear in: *Carbon*

Received Date: 10 November 2017

Revised Date: 14 March 2018

Accepted Date: 21 March 2018

Please cite this article as: N. López-Salas, M.L. Ferrer, M.C. Gutiérrez, J.L.G. Fierro, C. Cuadrado-Collados, J. Gandara-Loe, J. Silvestre-Albero, F. del Monte, Hydrogen-bond supramolecular hydrogels as efficient precursors in the preparation of freestanding 3D carbonaceous architectures containing BCNO nanocrystals and exhibiting a high CO_2/CH_4 adsorption ratio, *Carbon* (2018), doi: 10.1016/j.carbon.2018.03.066.

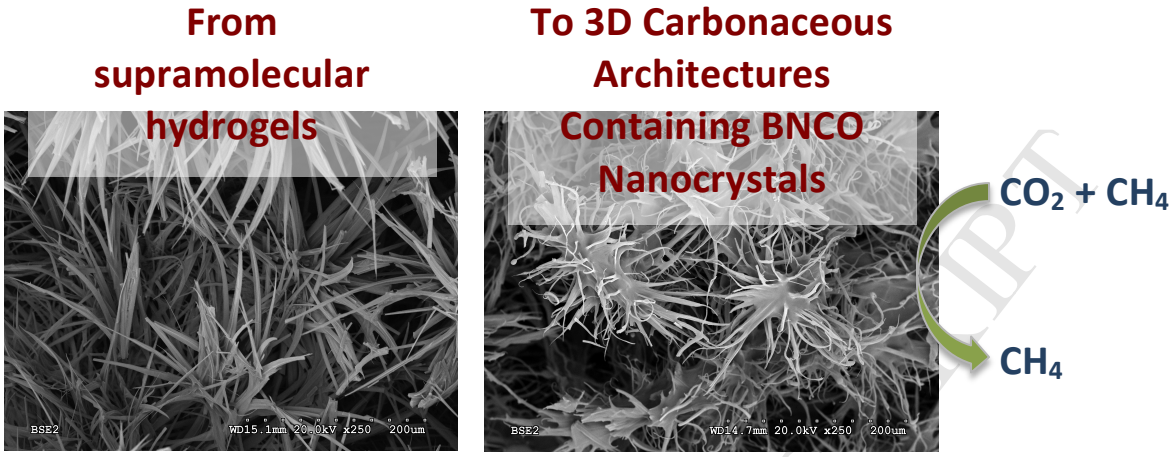

Hydrogen-Bond Supramolecular Hydrogels as Efficient Precursors in the Preparation of Freestanding 3D Carbonaceous Architectures Containing BCNO Nanocrystals and Exhibiting a High CO_2/CH_4 Adsorption Ratio

N. López-Salas,[a] M. L. Ferrer,[a] M. C. Gutiérrez,[a] J. L. G. Fierro,[b] C. Cuadrado-Collados,[c] J. Gandara-Loe,[c] J. Silvestre-Albero,[c] F. del Monte[a, *]

[a] *Materials Science Factory, Instituto de Ciencia de Materiales de Madrid-ICMM, Consejo Superior de Investigaciones Científicas-CSIC. Campus de Cantoblanco, 28049-Madrid (Spain).* [b] *Instituto de Catálisis y Petroleoquímica-ICP, Consejo Superior de Investigaciones Científicas-CSIC, Campus de Cantoblanco, 28049-Madrid (Spain).* [c] *Laboratorio de Materiales Avanzados, Departamento de Química Inorgánica-Instituto Universitario de Materiales, Universidad de Alicante. Ctra. San Vicente-Alicante s/n, E-03690 San Vicente del Raspeig (Spain)*

[*] Corresponding author. E-mail: delmonte@icmm.csic.es

ABSTRACT

Oxygen-enriched boron carbonitrides – known as boron carbon oxinitrides, BCNOs – have exhibited remarkable properties with numerous works reporting on their performance as phosphors and some few ones as H_2-adsorbents. However, the study of BCNOs capability for CO_2 uptaking has yet to be achieved. Herein, we have designed a simple process for preparation of freestanding three-dimensional (3D) BCNO structures via pyrolysis of supramolecular gels formed by H-bonding of melamine, boric acid and glucose. The 3D porous materials obtained by pyrolysis of supramolecular gels containing glucose exhibited a seaweed-like 3D structure formed by BCNO nanocrystals embedded within a carbonaceous matrix with a certain content of amorphous hydrogenated carbon. The particularly narrow porosities exhibited by these samples proved effective for CO_2 adsorption with uptakes of up to ca. 2 mmol/g at 25 °C. More interestingly, those samples prepared with high concentration of glucose behaved as molecular sieves and exhibited an excellent performance for CO_2–CH_4 separation, especially at low pressures with k_H values of up to $1.04 \cdot 10^3$.

1. INTRODUCTION

The discovery of two-dimensional (2D) materials is revolutionizing the field of materials science.[1, 2] Besides silicene, black phosphorus, metal oxides and hydroxides, transition metal dichalcogenides, or metal carbides, graphene-based materials as well as hexagonal-boron-nitride-based ones – *h*-BN, a graphene analogue so-called white graphene – are undoubtedly among the most interesting ones because, while sharing certain features like their 2D structure and an excellent mechanical strength, they exhibit a quite opposite behaviour with regard to their chemical and thermal stability – i.e. *h*-BN is air stable up to 1000 °C whereas graphene is not – as well as to their electrical conductivity – i.e. *h*-BN is an excellent insulator due to their wide energy band gaps (∼5-6 eV) whereas the electrical conductivity of graphene at room temperature is in range to that of some metals.

The blooming expectations created by graphene and *h*-BN motivated the exploration of the properties of borocarbonitrides (BCNs), another 2D material in the form of nanoplatelets that contain both graphene and BN domains.[3] Interestingly, BCNs have exhibited impressive surface and catalytic properties ascribed to the presence of active sites coming from defects in the carbon network – e.g. C sp^3 and/or Stone-Wales-Thrower defects. For instance, a remarkable performance has been reported for BCNs in both photocatalytic[4] and electrocatalytic[5] reactions as well as in the uptake of CO_2 and CH_4.[6, 7]

With regard to this latter application, oxygen-enriched BCNs – known as boron carbon oxinitrides, BCNOs – seems quite promising. Actually, BCNOs have exhibited an excellent performance in the uptake of H_2[8, 9] despite their most extended use is as phosphors.[10, 11, 12] It is worth noting that high uptakes of H_2 are also typical of *h*-BN[13] but, in BCNOs, it was ascribed to the presence of uniform and ultra-narrow micropores resulting from partial disorder between layers – i.e. as in turbostratic BN (*t*-BN).[14] Interestingly, we have been unable to find works reporting about BCNOs capability for CO_2 uptake.

Finally and before introducing our work, we would like to comment about the increased interest in up-scaling two-dimensional (2D) materials into freestanding three-dimensional (3D) ones because of the significant enhancement of the volumetric performance that may be of interest in certain applications.[15, 16] While the number of

strategies to obtain freestanding 3D architectures retaining the characteristic features of the original 2D materials for graphene includes both hard- and soft-templates as well as template-free approaches,[16a, 17] the chemical routes to obtain 3D *h*-BN and BCN architectures are mostly limited to the use of hard-templates[18] with just few examples using different procedures.[19] The challenge in this regard is designing simple and low-cost synthetic routes – hence suitable for large-scale production – of *h*-BNs, BCNs and/or BCNOs.

Herein, we describe a synthetic procedure for the preparation of 3D BCNO architectures taking advantage of the capability of some precursors commonly used in BCNO syntheses – e.g. melamine (M) – for supramolecular assembly. This approach has not been explored for BCNOs but one may find some few elegant works describing how carbon nitrides (CNs) can be obtained in the form of 3D architectures – e.g. hollow spheres and monoliths – upon calcination of supramolecular gels resulting from the molecular cooperative assembly between melamine and cyanuric acid.[20, 21] Actually, the number of acids with which M can form supramolecular gels is not limited to cyanuric acid,[22] and those with hydroxy benzoic acids[23] or gallic acid[24] are also representative examples. In our case, we obtained supramolecular gels composed of M, boric acid (B) and different glucose (G) contents, the pyrolysis of which – after freeze-drying – resulted in freestanding 3D structures. Among the different characterization techniques used in this work, TEM and FTIR spectroscopy proved particular effective to reveal the particular composition of pyrolyzed materials. Nitrogen adsorption isotherms confirmed the presence of narrow micropores characteristic of BCNO materials. Finally, we also studied the adsorption capacity of these materials for CO_2 as well as their suitability for CO_2–CH_4 separation purposes thanks to molecular sieving effects exerted by their above-mentioned narrow porosity.

2. EXPERIMENTAL

2.1. Materials

D-glucose (G), melamine (M) and boric acid (B) were purchased from Sigma-Aldrich and used as received. Water was distilled and deionized.

2.2. Preparation of hydrogels and carbons

The starting solutions were prepared at 90 °C upon mixing 20 mg of M, 29 mg of B and a certain amount of G – e.g. nil, 60 or 120 mg – in 1 ml of distilled water. Supramolecular gels – e.g. SG_{MB}, SG_{MBG1} and SG_{MBG2}, coming from solutions containing nil, 60 or 120 mg of G, respectively – were obtained upon cooling down the transparent solutions from 90 °C to room temperature. SG_{MB}, SG_{MBG1} and SG_{MBG2} were stored at room temperature over 24 h and then submitted to a freeze-drying process. The resulting hydrogels were stored at 25 °C under vacuum over 72 h and then, pyrolyzed at 1000 °C over 1 h under a N_2 atmosphere (heating ramp was 10 °C/min). The resulting samples were named as $BCNO_{MB}$, $BCNO_{MBG1}$ and $BCNO_{MBG2}$, depending on the G content in the original hydrogel.

2.3. Sample characterization

Differential scanning calorimetry (DSC) was performed with a TA Instruments Model DSC Q-100 system, under a nitrogen atmosphere. Scans were run using aluminum pans in a sealed furnace, first stabilized at 20 °C and then cooled to -90 °C before heating up to 90 °C at a heating rate of 5 °C/min. Thermal analysis from 25 to 1000 °C was carried out using a TA Instruments Model ATD/DSC/TG Q600, using a heating ramp of 10 °C/min and in a N_2 atmosphere. Fourier transform infrared (FTIR) spectroscopy was performed in a FTIR spectrometer (Bruker Model IFS66v). Samples were mixed with KBr and processed in the form of disks. Then they were analyzed in transmission mode from 500 to 4000 cm^{-1}. Scanning electron microscopy (SEM) was performed in a Hitachi S-3000N microscope. Samples were coated with a 15nm gold layer. Photos were taken under high vacuum conditions, at a width distance of 15 mm, recording the signal of back-scattered electrons and using 20 keV as the electron beam energy. Energy-dispersive X-ray spectroscopy was carried out using a coupled Oxford Instruments EDX analyzer. Elemental mapping (B, C, N, O) was performed in a FE-SEM FEI Nova NANOSEM 230 using an electron beam energy of 5 keV, a width distance of 6 mm and a magnification of 1.6kx for $BCNO_{MB}$ sample and 3kx magnification for $BCNO_{MBG1}$ and $BCNO_{MBG2}$. Secondary electron micrographs of the analyzed spot were also taken for the record. High-resolution transmission electron microscopy (HRTEM) was carried out using a TEM/STEM (JEOL 2100F) operating at 200KV. Micrographs were recorded at high magnification (400kx to 600kx) in order to detect the presence of nanocrystals in the materials. Dark field micrographs were recorded at 100kx. X-ray

diffraction patterns were recorded using a powder diffractometre Bruker D8 Advance with Cu Kα radiation and a lynxeye detector. Raman spectra were recorded with a Renishaw inVia Raman microscope using irradiation at 514 nm (100% laser power, 2 mW power, 10 accumulations, and an exposure time of 10 s). X-Ray Photoelectron (XPS) spectroscopy surface analysis was performed in a VG ESCALAB 200R electron spectrometer equipped with a hemispherical electron analyser and an Al Kα (hν=1486.6 eV, 1 eV=$1.6302 \cdot 10^{-19}$ J) 100 Watts X-ray source. Samples were carbon glued on 8 mm diameter stainless steel troughs mounted on a sample rod placed in the pre-treatment chamber and degassed for 0.5 h prior to being transferred to the analysis chamber. The base pressure in the analysis chamber was maintained below $3 \cdot 10^{-9}$ mbar during data acquisition. The pass energy of the analyser was set at 50 eV. The binding energies were referenced to the binding energy of the C1s core-level spectrum at 284.8 eV. Data processing was performed with the XPS peak program, the spectra were decomposed with the least squares fitting routine provided with the software with Gaussian/Lorentzian (90/10) product function and after subtracting a Shirley background. Atomic fractions were calculated using peak areas normalized on the basis of sensitivity factors provided by the manufacturer. Hg Porosimetry was performed in a Micromeritics autopore IV 9500. N_2 adsorption/desorption isotherms at -196 °C were conducted using an ASAP 2020 from Micromeritics system on samples thermally treated overnight at 200 °C prior to N_2 gas adsorption. The pore size distribution (PSD) for these samples was estimated from the QSDFT model applied to the N_2 adsorption data, assuming slit-shaped pore geometry. Brunauer-Emmett-Teller (BET) theory was used to calculate the specific surface areas (S_{BET}) and the microporous volume (V_{N2}) was calculated from the Dubinin-Radushkevich (DR) equation. The narrow micropore volume (V_{CO2}) was calculated after applying the DR equation to the CO_2 adsorption data at 0 °C. H_2 adsorption/desorption isotherms at -196 °C, CO_2 adsorption/desorption isotherms at 0 and 25 °C, and CH_4 adsorption/desorption isotherms at 25 °C were performed in a homemade fully automated manometric equipment designed and constructed by the Advanced Materials Group (LMA), now commercialized by Gas to Materials Technologies (www.g2mtech.com). Before adsorption measurements, samples were outgassed at 200 °C over 12 h. The Henry´s constants (K_H) were calculated by fitting the adsorption

data to a Virial-type equation, following the procedure described elsewhere.[25] Thus, the Henry´s law selectivity for gas component CO_2 (i) over CH_4 (j) at a given temperature was calculated using the equation $S_{ij} = K_{Hi}/K_{Hj}$. Selectivity values were also calculated at equilibrium conditions as the ratio between CO_2 and CH_4 adsorption at low pressures (266 mbar) and near atmospheric conditions (933 mbar).

3. RESULTS AND DISCUSSION

3.1. Preparation of freestanding 3D architectures

As mentioned above, we have explored the preparation of 3D BCNO architectures by pyrolysis of hydrogels. Thus, we first mixed M with B in an aqueous solution (see Table S1 for details) to obtain a supramolecular gel (see SG_{MB} in Figure 1a) composed of crystalline melamine diborate fibres[26, 27, 28] (see Figure S1, and FTIR and XRD in Figures S2 and S3), the stacking of which after freeze-drying resulted in the formation of a pseudo-freestanding-3D architecture with a fragile fibre-like network structure prone to collapse upon handling (Figure 1b). This scenario changed when the aqueous solutions of M and B also contained a certain amount of G (see SG_{MBG1} and SG_{MBG2} in Figure 1 and S1, see also Table S1 for experimental details). In structural terms, the freestanding 3D architectures of SG_{MBG1} and SG_{MBG2} evolved from the above-mentioned stack-of-crystalline-fibres structure obtained from M and B into a seaweed-like supramolecular structure interconnected via hydrogen-bonding (Figure 1). In these latter cases, FTIR spectroscopy confirmed the formation of the hydrogen-bond supramolecular structures between M and B – i.e. with bands at 3524, 3498 and 3417 cm^{-1} corresponding to amine groups of M in melamine diborate (Figure S2) – although XRD revealed a significant decrease of their crystalline features most likely as consequence of G participation in the original hydrogen-bond supramolecular structures formed between M and B (Figure S3). The presence of a single melting point at every DSC scan – just appearing at lower temperatures along with the increase of G content (Figure S4) – further corroborated the participation of G in the hydrogen-bond supramolecular structure. At this stage, it is worth noting that aqueous solutions of M and B, as well as of M, B and G have been used for the preparation of BNCs[29] and BCNOs,[30] but always upon thermal treatment of a precipitate rather than of a hydrogel. In our case, the use of solutions that contain glucose was critical for

transitioning from a non-branched-stack-of-fibres structure to the branched one that is characteristic of hydrogels (Figure 1).[31]

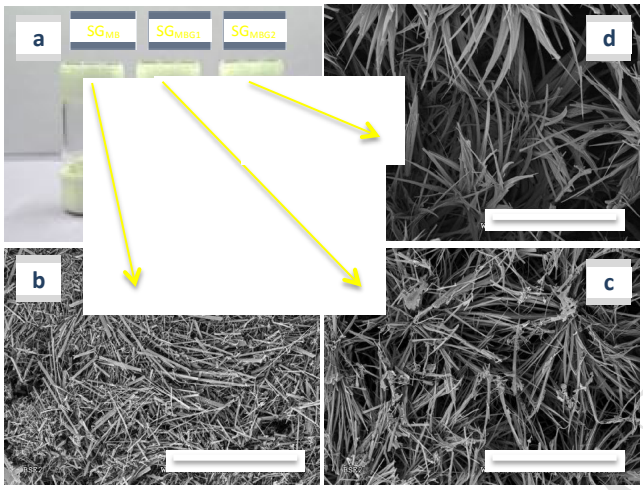

Figure 1 – (a) From left to right, pictures of the supramolecular gels obtained by mixing M and B (SG_{MB}), or M, B and glucose (SG_{MBG1} and SG_{MBG2}). SEM micrographs of SG_{MB} (b), SG_{MBG1} (c) and SG_{MBG2} (d) after freeze-drying. Bars are 200 µm in every case.

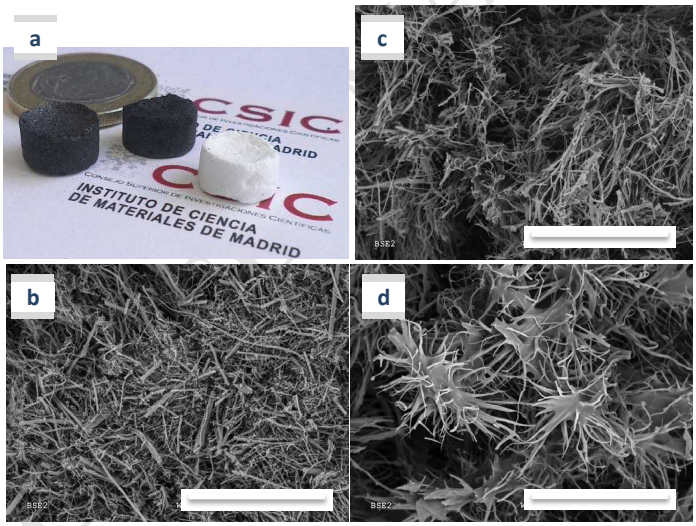

Figure 2 – (a) From left to right, pictures of the free-standing-monoliths $BCNO_{MBG2}$, $BCNO_{MBG1}$ and $BCNO_{MB}$ obtained after thermal treatment. SEM micrographs of $BCNO_{MB}$ (b), $BCNO_{MBG1}$ (c) and $BCNO_{MBG2}$ (d). Bars are 200 µm in every case.

The network structure of the samples obtained after thermal treatment at 1000 °C and under nitrogen atmosphere resembled that of the original ones – i.e. fibre-like for that coming from M and B, and seaweed-like for those coming from M, B and G (see, respectively, $BCNO_{MB}$, $BCNO_{MBG1}$ and $BCNO_{MBG2}$ in Figure 2). Actually, data coming

from Hg porosimetry could only be obtained for $BCNO_{MBG1}$ and $BCNO_{MBG2}$ (Table S4 and Figure S5) but not for $BCNO_{MB}$ given the weakness of its non-branched-stack-of-fibres structure. Besides these structural differences, the colour of the freestanding 3D architectures also differed – i.e. white for $BCNO_{MB}$, black for $BCNO_{MBG1}$ and $BCNO_{MBG2}$, see Figure 2 – in agreement with the increased carbon content found in those samples prepared with G – see elemental mapping in Figure S6 and data obtained from energy-dispersive X-ray spectroscopy (EDX) in Table S2. It is worth noting that hydrogels conversion into BCNOs in the form of freestanding 3D architectures was achieved with yields of ca. 30 % (Figure S7) that were in range or slightly below the best yields found in previous works for achievement of carbons via direct carbonization of biomass and ionic liquids – ca. 40 and 30%, respectively[32, 33] – and a bit further below those of aromatic polymers – e.g. 60% for polyimides[34] – or hydrogels.[35]

3.2. Chemical composition and crystalline features of freestanding 3D architectures

XRD was used to further investigate whether the materials resulting after thermal treatment were BCNOs (Figure 3). The XRD patterns were similar for all samples and exhibited peaks centred at ca. 26° and 43° (in 2θ), corresponding to (002) interlayer and (101), (100) in-plane reflections of disordered BN phases – e.g. turbostratic BN, *t*-BN – that are characteristic of BCNO samples.[8-12, 14] The strong broadening of the diffraction peaks was indicative of the nanometric dimensions of *t*-BN crystallites. HRTEM micrographs further confirmed the presence of nanocrystals embedded within an amorphous matrix (see also TEM dark field images in Figure 4). The lattice spacing obtained from HRTEM images for these nanocrystals was 0.34 nm, this is larger than the 0.33 nm value for the (002) planes of *h*-BN and in agreement with those reported for *t*-BN (Figure 4).[10, 11, 12]

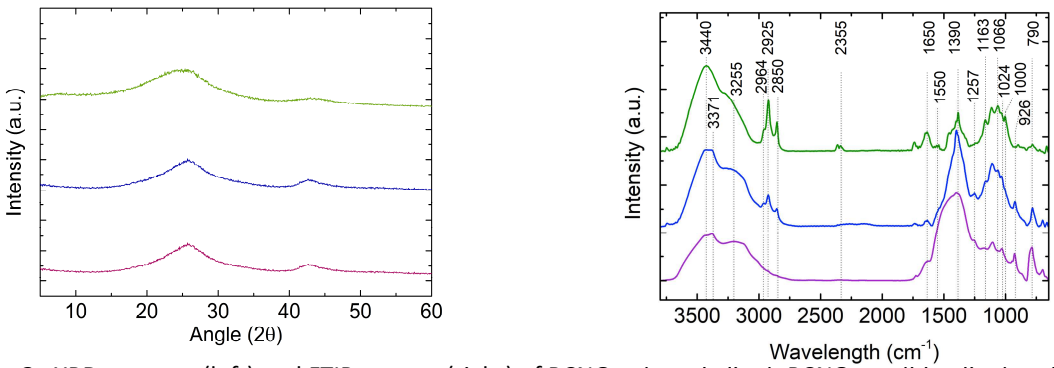

Figure 3 –XRD patterns (left) and FTIR spectra (right) of $BCNO_{MB}$ (purple line), $BCNO_{MBG1}$ (blue line) and $BCNO_{MBG2}$ (green line).

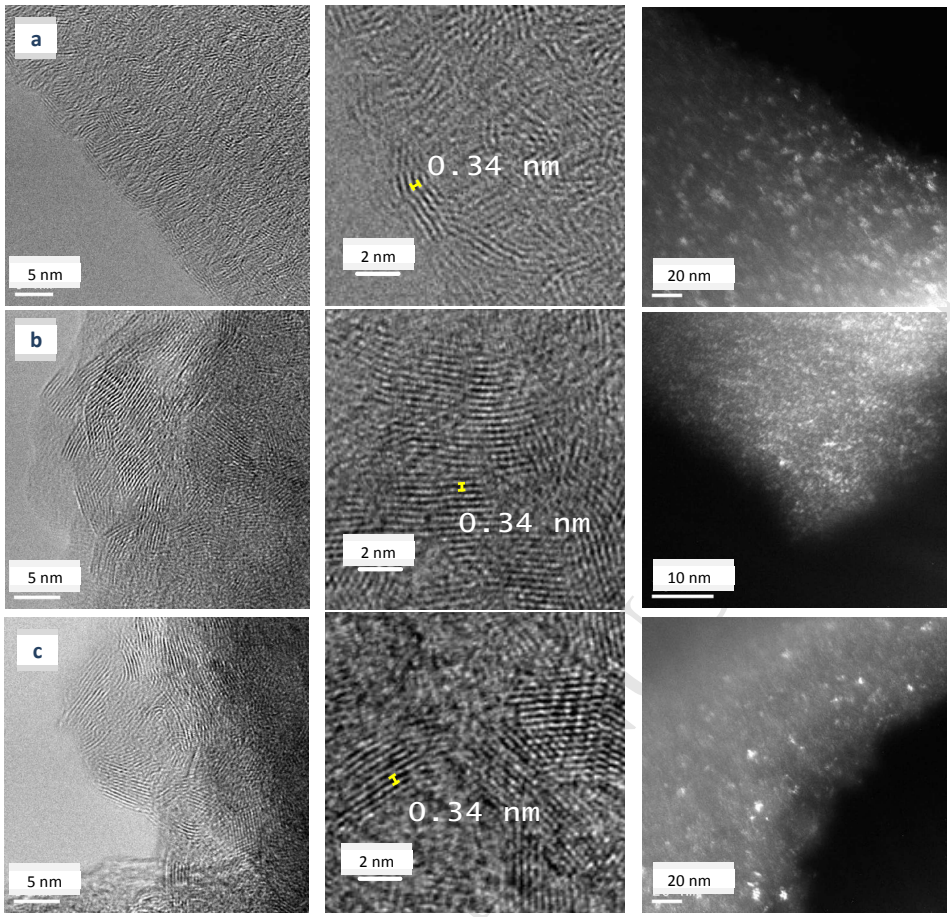

Figure 4 – From left to right, TEM, HRTEM and dark field images of (a) $BCNO_{MB}$, (b) $BCNO_{MBG1}$ and (c) $BCNO_{MBG2}$.

The FTIR spectra of $BCNO_{MB}$, $BCNO_{MBG1}$ and $BCNO_{MBG2}$ also exhibited the typical bands observed for BCNO samples (Figure 3). Thus, bands at 790 and 1390 cm^{-1} were assigned to the in-plane stretching and out-of-plane bending vibrations of *h*-BN,[12, 30] whereas bands assigned to B-C at 1163 cm^{-1} and to the typical stretching modes of C–N heterocycles – e.g. C–N, C=N and C≡N at, respectively, 1257, 1550 and 2355 cm^{-1} – indicated the participation of C in the structure of every sample.[36, 37] Stretching bands of N–B–O groups – induced by the oxidation of N–B bonds – observed within the 900-1100 cm^{-1} range further corroborated this issue.[37] Broad bands ranging from 3000 to 3500 cm^{-1} have been assigned to O–H and N–H.[38] Interestingly, neither XRD – see XRD patterns above – nor FTIR spectroscopy revealed the presence of B_2O_3 in our samples – with vibrations in the FTIR spectrum at 644, 734, and 1448 cm^{-1} originated from B-O bonds and at 885 cm^{-1} from the stretching vibration of tetrahedral BO_4^- – despite it is a typical by-product observed in most of works using precursors similar to

ours but in the form of precipitate. [30, 39] The FTIR spectra also exhibited some interesting bands at 1650 cm^{-1} (for every sample) and at 2850, 2925, and 2964 cm^{-1} (only for $BCNO_{MBG1}$ and $BCNO_{MBG2}$). The former was assigned to C=C groups[30, 37] and revealed the presence of a carbon network. The latter were assigned to C–H stretching vibrations – i.e. in particular, to the sp^3 symmetric and asymmetric mode of CH_2, and to the sp^3 asymmetric mode of CH_3, respectively – and revealed the presence of amorphous hydrogenated carbons (*a*-C:H).[40, 41] These results allowed us identifying the nature of the matrix surrounding the BCNO nanocrystals – see HRTEM images in Figure 4 – as either amorphous carbon for $BCNO_{MB}$ or a mixture of *a*-C:H and amorphous carbon for $BCNO_{MBG1}$ and $BCNO_{MBG2}$.

XPS spectra confirmed not only the presence of B, N, C and O elements but also their combination in the form of BCNO (Figure 5 and Table S3). Thus, the B1s signal was deconvoluted into two peaks assigned to B–C and B–N (at 191.6 and 192.1 eV, respectively),[4, 42, 43, 44] the relative intensity of which evolved along with the G content in the original hydrogel used as precursor. Meanwhile, the N1s spectrum was deconvoluted into three peaks at ca. 398.5, 400.0 and 401.6 eV, and assigned to B–N, C–N and graphitic (or quaternary) N, respectively.[40, 45] The O1s spectrum was also deconvoluted into three peaks at 531.3, 532.4 and 533.8 eV, and assigned to N–O, C–O and B–O (in N–B–O groups), respectively.[36, 40, 46] Finally, the C1s spectrum was deconvoluted into three peaks at 284.8, 286.3 and 287.8 eV, and assigned to graphitic C=C, C–O, and C–N, respectively.[36, 45] Attempts to confirm the presence of C with sp^3 hybridization characteristic of *a*-C:H in $BCNO_{MBG1}$ and $BCNO_{MBG2}$ were performed upon deconvolution of their respective C1s spectra into four peaks at 284.8, 285.5, 286.3 and 287.8 eV, corresponding to, respectively, graphitic C=C, C sp^3, C–O, and C–N (Figure S8). Whereas the peak assigned to C sp^3 was observed in both $BCNO_{MBG1}$ and $BCNO_{MBG2}$,[47] its intensity evolution provided less conclusive results than those obtained from FTIR. Nonetheless, it is our belief that FTIR spectroscopy was quite reliable for studying the evolution of C–H groups, more so than XPS spectroscopy where peak deconvolution is required for assignment.

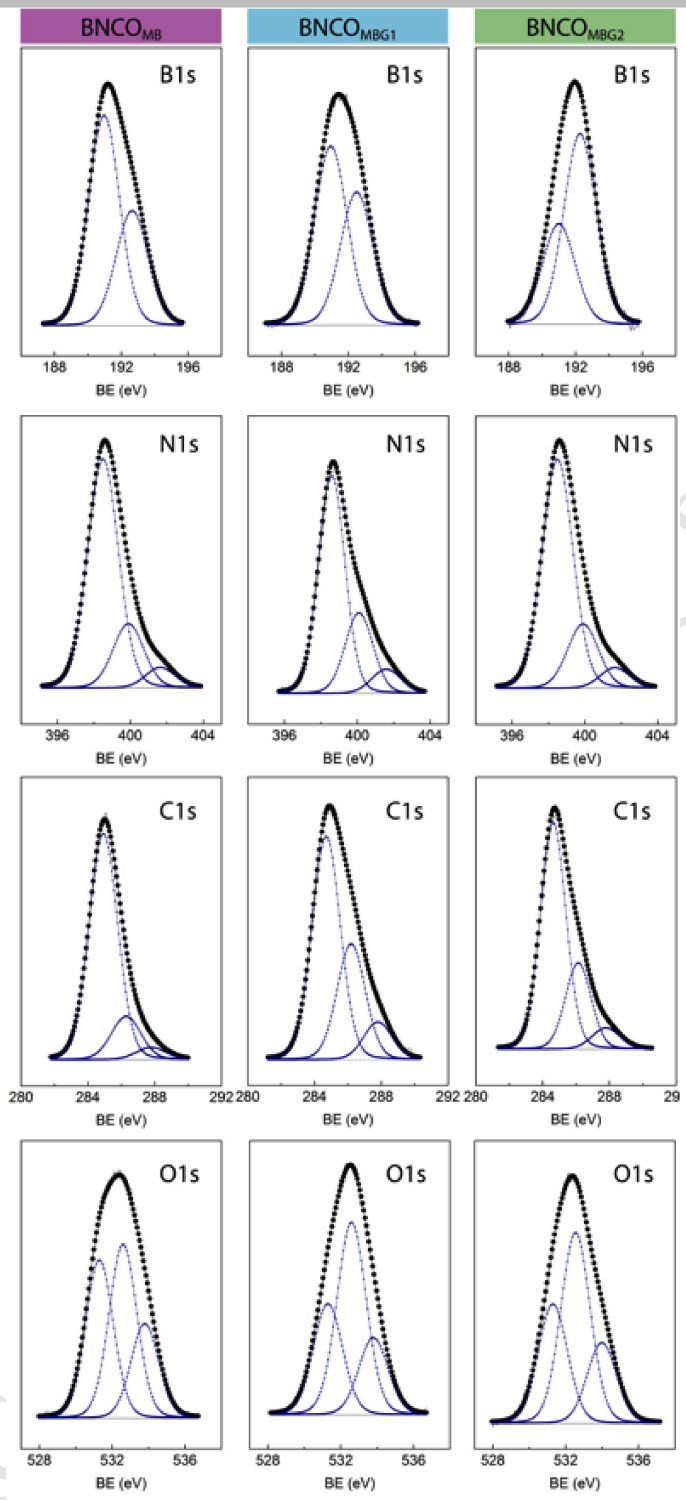

Figure 5 – B1s, N1s, C1s and O1s XPS deconvoluted peaks of BCNO$_{MB}$, BCNO$_{MBG1}$ and BCNO$_{MBG2}$. The binding energies were referenced to the binding energy of the C1s core-level spectrum at 284.8 eV. Data processing was performed with the XPS peak program, the spectra were decomposed with the least squares fitting routine provided with the software with Gaussian/Lorentzian (90/10) product function and after subtracting a Shirley background. Atomic fractions were calculated using peak areas normalized on the basis of sensitivity factors provided by the manufacturer.

3.3. Gas adsorption of freestanding 3D architectures

Next, we investigated the sorption capabilities of $BCNO_{MB}$, $BCNO_{MBG1}$ and $BCNO_{MBG2}$. Thus, we first studied N_2 adsorption at -196 °C (Figure 6, Figure S9 and Table 1). According to the IUPAC classification, the N_2 adsorption/desorption isotherm of $BCNO_{MB}$ was type IV with adsorption and desorption branches parallel to each other and almost horizontal in the region of medium-high pressures – i.e. H4-type hysteresis loop, and with a steep adsorption in the low-pressure region that reveals the presence of micropores. The Brunauer–Emmett–Teller surface area (S_{BET}) experienced a significant decrease for samples prepared from G-containing hydrogels – more so in $BCNO_{MBG2}$ than in $BCNO_{MBG1}$. Actually, $BCNO_{MBG2}$ exhibited a negligible surface area from N_2 adsorption at -196 °C. It is worth noting that negligible N_2 adsorption has been previously observed in a number of different samples with narrow micropores – e.g. zeolites, MOFs, carbons, etc. – due to diffusional restrictions typically occurring at cryogenic temperatures that limit the gas entrance into such a narrow micropores.[48, 49, 50, 51, 52, 53, 54, 55]

H_2 adsorption at -196 °C further corroborated this occurrence. As mentioned in the introduction, BCNOs have demonstrated a remarkable performance for H_2 uptake, in range to those exhibited by *h*-BN – up to 1.5 wt% for BCNOs and 2.6 wt% for BNCs, at 1 bar and -196 °C.[6, 9] In our case, the H_2 adsorption capacity of our samples was slightly below those figures but yet in range to previous works reporting on both BCNOs and BNCs (Figure 6).[8, 13] The highest H_2 adsorption capacity was found for $BCNO_{MBG1}$, then decreased for $BCNO_{MB}$ and further decreased for $BCNO_{MBG2}$ – ca. 0.80, 0.65 and 0.50 wt%, respectively. It is worth noting how the adsorption capability of $BCNO_{MBG1}$ now surpassed that of $BCNO_{MB}$, thus revealing the role played by the kinetic diameter of the gas – 0.364 nm for N_2 versus 0.289 nm for H_2 – in the occurrence or not of restricted diffusion through narrow micropores.[50, 51] According to this reasoning, the low H_2 adsorption capability observed for $BCNO_{MBG2}$ indicated that micropores in this particular sample – or, at least, micropore entrance – were yet too narrow to allow the entry of H_2 without kinetic restrictions.

Considering that neither N_2 nor H_2 adsorption isotherms carried out at cryogenic temperatures provided a reliable assessment of the textural properties of $BCNO_{MBG2}$, next adsorption analyses were performed using CO_2 at non-cryogenic

temperatures. It is worth noting that the kinetic diameter of CO_2 – e.g. 0.33 nm – is just slightly smaller than that of N_2 – e.g. 0.36 nm – and even larger than that of H_2 – e.g. 0.29 nm – so, rather than the gas nature, the main difference between previous N_2 and H_2 adsorption experiments, and the following CO_2 adsorption ones was the use of temperatures where kinetic restrictions could be considered negligible. Actually, CO_2 adsorptions at 0 and/or 25 °C have been widely used to evaluate the presence of narrow constrictions usually inaccessible to N_2 at cryogenic temperatures.[48-55, 56, 57] Interestingly, the trend found in the CO_2 adsorption/desorption isotherms was the opposite than that for N_2 adsorption, with CO_2 adsorption at 1 bar and 25 °C increasing from ca. 1.2 mmol/g for $BCNO_{MB}$ to ca. 1.9 mmol/g for both $BCNO_{MBG1}$ and $BCNO_{MBG2}$ (Figure 7, Table 2). The occurrence of pseudo-high CO_2 adsorption in samples exhibiting negligible N_2 adsorption confirmed the presence of a narrow microporous network in both $BCNO_{MBG1}$ and $BCNO_{MBG2}$ and hence, their capability to work as molecular sieves for gas separation purposes. An overall analysis of the adsorption isotherms of $BCNO_{MBG1}$ and $BCNO_{MBG2}$ – i.e. with higher N_2- and H_2-adsorption capabilities at -196 °C for $BCNO_{MBG1}$ than for $BCNO_{MBG2}$, whereas the CO_2 adsorption at 0-25 °C was similar for both of them – revealed how, despite their similarities with regard to the total pore volume, the pore entrance was narrower in $BCNO_{MBG2}$ than in $BCNO_{MBG1}$, thus anticipating a more efficient molecular-sieve behaviour in the former sample.

	S_{BET} (m^2/g)[a]	Total Volume (cm^3/g)[b]	Micropore Volume (N_2) (cm^3/g)[c]	Micropore Volume (CO_2) (cm^3/g)[d]	Mean pore diameter	
					QSDFT (nm)[e]	Hg porosimetry (μm)[f]
$BCNO_{MB}$	347	0.19	0.13	0.15	0.7/1.2/3.4	--
$BCNO_{MBG1}$	53	0.03	0.02	0.18	--/1.2/3.2	25.63
$BCNO_{MBG2}$	3	0.00	0.00	0.20	--/--/--	38.53

[a] Applying BET equation to the N_2 adsorption/desorption isotherms; [b] Determined using the DR equation applied to the N_2 adsorption data; [c] Determined at p/p_0 ~ 0.99; [d] Determined using the DR equation applied to the CO_2 adsorption data; [e] mean pore diameter estimated from the QSDFT model (equilibrium model for slit-shaped carbons) and [f] mean pore diameter obtained by 4V/A equation obtained from Hg porosimetry data.

Table 1: Summary of data obtained from both N_2 adsorption/desorption isotherms at -196 °C and CO_2 adsorption/desorption isotherms at 0 °C for $BCNO_{MB}$, $BCNO_{MBG1}$ and $BCNO_{MBG2}$. Data with regard to the macropore size of $BCNO_{MBG1}$ and $BCNO_{MBG2}$ (obtained from Hg porosimetry) is also included.

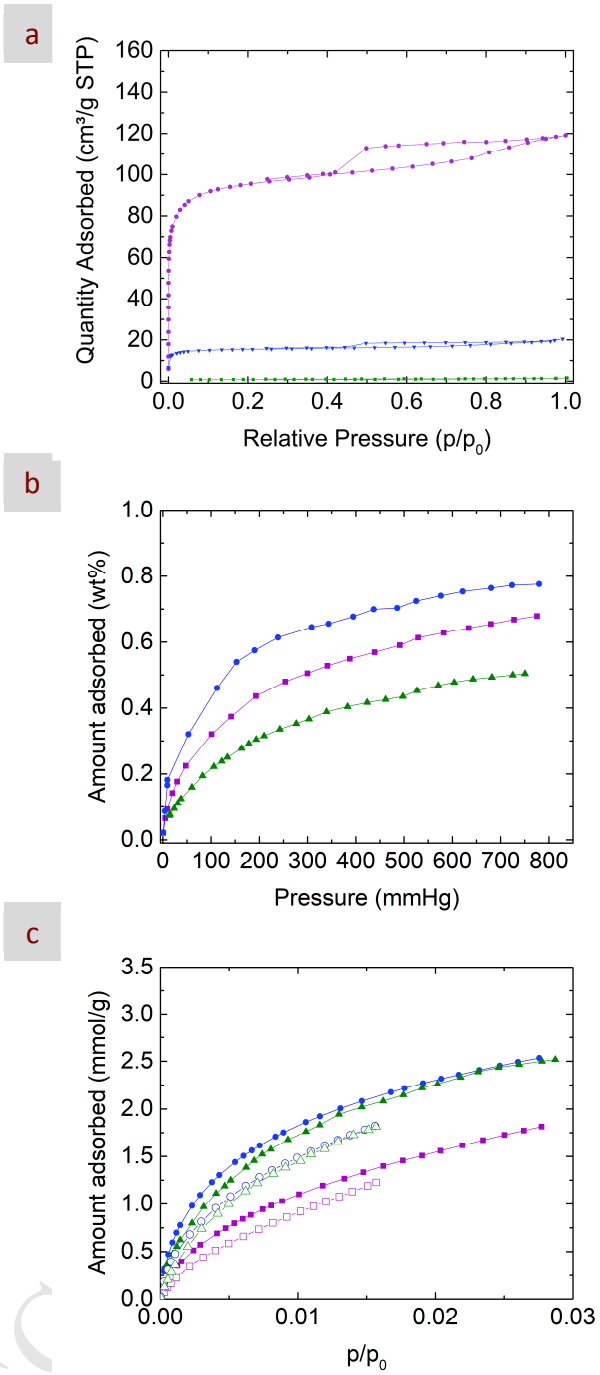

Figure 6 – Adsorption isotherms of $BCNO_{MB}$ (purple line), $BCNO_{MBG1}$ (blue line) and $BCNO_{MBG2}$ (green line) using (a) N_2 at -196 °C, (b) H_2 at -196 °C, and (c) CO_2 at 0 (solid symbols) and 25 °C (open symbols).

It is worth noting that CO_2 adsorption capability of our samples was not in the upper range of previously reported CO_2 sorbents exhibiting high sorption capacities[58, 59, 60, 61, 62, 63] but it was indeed of sorbents used for gas separation purposes where the figure of merit is either CO_2 versus N_2 adsorption[55, 64, 65, 66, 67, 68] or CO_2 versus CH_4 adsorption[55, 64, 68, 69] rather than neat CO_2 adsorption.[70] The molecular sieving properties of these samples, preferentially sample $BCNO_{MBG2}$, can be further noticed in

Table 1 with figures for narrow micropore volume (V_{CO2}) being larger than for total micropore volume (V_{N2}).

Based on this, we further explored the selectivity of CO_2 versus CH_4 adsorption at 25 °C, at equilibrium conditions and at low as well as near atmospheric pressures – e.g. 266 and 933 mbar, respectively (Figure 7, Table 2). In this case, selectivity was just obtained as the ratio between CO_2 and CH_4 adsorptions reached at equilibrium at the above-mentioned pressures. Selectivity increased from $BCNO_{MB}$ to $BCNO_{MBG1}$ up to $BCNO_{MBG2}$ confirming the increased presence of narrow micropores in which selective adsorption of CO_2 was governed by molecular sieve effects, so that gases having small kinetic diameters are preferentially adsorbed over those having large ones – e.g. 0.33 nm for CO_2 versus 0.38 nm for CH_4. At equilibrium, the selectivity figures found for both $BCNO_{MBG1}$ and $BCNO_{MBG2}$ were in range to those found for some of the best adsorbents reported to date.

	Reference	CO_2-uptake (mmol/g)	CO_2/CH_4 Selectivity		
			Equilibrium – 933 mbar	Henry	Equilibrium – 266 mbar
$BCNO_{MBG1}$ [a]	This work	1.5	6.7	111	17.8
$BCNO_{MBG2}$ [a]	This work	1.5	15	1.04×10^3	86
Porous Carbon C125-220 [a]	55	2.8	10.8	4×10^4	
MIL-100 [b]	60	7.5	2.8	585	
CPC-550 [a]	61	5.8	9.5	12	
SIFSIX-2-Cu-i	62	5.4	31.7		
PINK [c]	63	4.1	32		
ZIF-78 [a]	64	2.2	10.2		6
PPN-81 [d]	68	1.9	29		
Zeolite 5 [b]	72	2.6	8.7	195.6	
H-b-Zeolite [b]	73			28.8	
ZrPOF-EA [a]	74	0.95	17.3		
BILP-2 [a]	75	3.4	11.6	12	
MOPI-IV [a]	76	2.3	5.7	9	
APTMS@Ph–PMO [a]	77	2.5	5	26.1	7

Table 2: CO_2 uptake at 1 bar and 25 °C, and CO_2–CH_4 selectivity of $BCNO_{MBG1}$ and $BCNO_{MBG2}$ at near ambient (under equilibrium conditions, 933 mbar) and at low (obtained either from Henry constants or under equilibrium conditions, 266 mbar) pressures. Data from different works are included for comparison. In these latter cases, it is worth noting that measurements were carried out at either ([a]) 25, ([b]) 30, ([c]) 0, or ([d]) 22 °C.

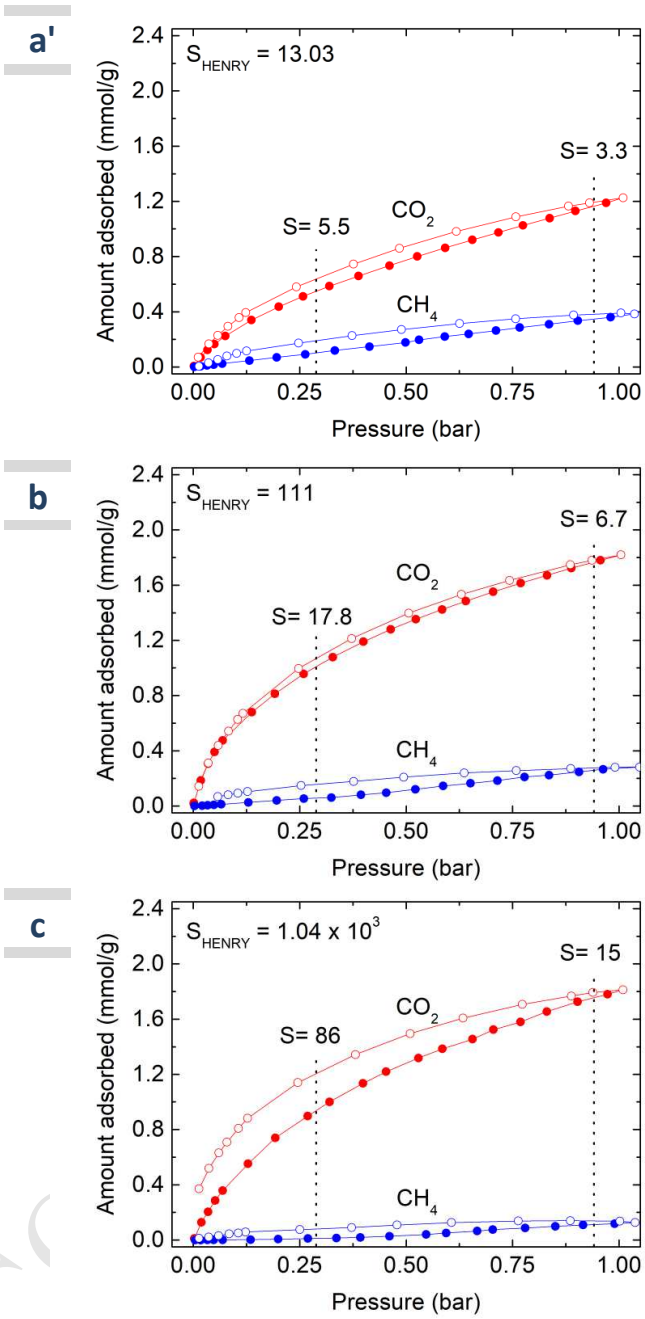

Figure 7 – CO_2 and CH_4 adsorption isotherms at 25 °C of (a) $BCNO_{MB}$, (b) $BCNO_{MBG1}$ and (c) $BCNO_{MBG2}$.

Nonetheless, it is well known that a large selectivity for CO_2 over other components of a gas mixture is particularly interesting in low-pressure post-combustion applications where the flue gas usually contains less than 15% of CO_2. For this reason, we also calculated the adsorption selectivity in a region more

representative of flue-gas streams characteristic of post-combustion and natural gas fields, this is at 266 mbars. The selectivity found in this region of low partial pressure was even more remarkable than at atmospheric pressure, with figures approaching 18 for $BCNO_{MBG1}$ and up to 86 for $BCNO_{MBG2}$. Besides the isotherm screening to obtain a direct measurement of the gas adsorption selectivity at low partial pressures, the Henry's law constant – e.g. k_H, related to the gas–adsorbent affinity at infinite dilution[71] – can also provide an interesting assessment of gas–solid interactions. Thus, the CO_2–CH_4 selectivities calculated for $BCNO_{MBG1}$ and $BCNO_{MBG2}$ from their respective k_H values were again remarkable, in the upper range of figures found for some of the most efficient adsorbents reported to date – e.g. see data in Table 2 for porous carbons, POFs, zeolites and MOFs.[55, 60, 61, 64, 68, 72, 73, 74, 75, 76, 77]

4. CONCLUSIONS

Our findings provide a simple and low-cost synthetic process for preparation of freestanding 3D BCNO structures via pyrolysis of supramolecular gels formed by H-bonding of M, B and G. The presence of G allowed transitioning from the non-branched-stack-of-fibres structure obtained for SGMB to the branched one – characteristic of hydrogels – obtained for SG_{MBG1} and SG_{MBG2}. The network structure of the samples obtained after pyrolysis resembled that of the original ones. Particularly interesting in compositional terms were the seaweed-like 3D architectures obtained from supramolecular gels containing glucose, with BCNO nanocrystals embedded within a carbonaceous matrix with a certain content of *a*-C:H. The particularly narrow porosities exhibited by these samples proved effective for CO_2 adsorption. More interestingly, molecular sieving effects in $BCNO_{MBG1}$ and $BCNO_{MBG2}$ provided outstanding figures for CO_2–CH_4 separation both in equilibrium and using the Henry's law constant. The latter were substantially remarkable, being in range or even above figures obtained for some of the best adsorbents reported to date despite the synthesis of our materials offer significant advantages in economical terms – i.e. quite easy to prepare without time consuming synthetic steps and from low-cost precursors.

5. APPENDIX A. SUPPLEMENTARY DATA

Supplementary data related to this article can be found at xxx.

ACKNOWLEDGEMENTS. This work was supported by MINECO/FEDER (Project Numbers MAT2015-68639-R and MAT2016-80285-P). N. López-Salas also acknowledges MINECO/FEDER for a FPI research contract. C. Cuadrado-Collados and J. Gandara-Loe acknowledge UA and GV (GRISOLIAP/2016/089) for their respective research contracts.

REFERENCES

[1] Novoselov, K. S.; Geim1, A. K.; Morozov, S. V.; Jiang, D.; Katsnelson, M. I.; Grigorieva, I. V.; Dubonos, S. V.; Firso, A. A. Two-dimensional gas of massless Dirac fermions in graphene. *Nature*, **2005**, *438*, 197–200.

[2] Kubota, Y.; Watanabe, K.; Tsuda, O.; Taniguchi, T. Deep ultraviolet light-emitting hexagonal boron nitride synthesized at atmospheric pressure**.** *Science*, **2007**, *317*, 932–934.

[3] Kumar, N.; Moses, K.; Pramoda, K.; Shirodkar, S. N.; Mishra, A. K.; Waghmare, U. V.; Sundaresana, A.; Rao, C. N. R. Borocarbonitrides, BxCyNz. *J. Mater. Chem. A* **2013**, *1*, 5806–5821

[4] Huang, C.; Chen, C.; Zhang, M.; Lin, L.; Ye, X.; Lin, S.; Antonietti, M.; Wang, X. Carbon-doped BN nanosheets for metal-free photoredox catalysis. *Nat. Commun.* **2015**, *6*. Article number: 7698

[5] Chhetri, M.; Maitra, S.; Chakraborty, H.; Waghmare, U. V.; Rao, C. N. R. Superior performance of borocarbonitrides, BxNyCz, as stable, low-cost metal-free electrocatalysts for the hydrogen evolution reaction. *Energy Environ. Sci.* **2016**, *9*, 95–101.

[6] Raidongia, K.; Nag, A.; Hembram, K. P. S. S.; Waghmare, U. V.; Datta, R.; Rao, C. N. R. BCN: A Graphene Analogue with Remarkable Adsorptive Properties. *Chem. Eur. J.* **2010**, *16*, 149–157.

[7] Kumar, N.; Subrahmanyam, K. S.; Chaturbedy, P.; Raidongia, K.; Govindaraj, A.; Hembram, K. P. S. S.; Mishra, A. K.; Waghmare, U. V.; Rao, C. N. R. Remarkable Uptake of CO_2 and CH_4 by Graphene-Like Borocarbonitrides, BxCyNz. *ChemSusChem* **2011**, *4*, 1662–1670.

[8] Portehault, D.; Giordano, C.; Gervais, C.; Senkovska, I.; Kaskel, S.; Sanchez, C.; Antonietti, M. High-Surface-Area Nanoporous Boron Carbon Nitrides for Hydrogen Storage. *Adv. Funct. Mater.* **2010**, *20*, 1827–1833.

[9] Weng, Q.; Wang, X.; Wang, X.; Liu, D.; Jiang, X.; Zhi, C.; Bando, Y.; Golberg, D. Preparation and Hydrogen Sorption Performances of BCNO Porous Microbelts with Ultra-Narrow and Tunable Pore Widths. *Chem. Asian J.* **2013**, *8*, 2936–2939.

[10] Ogi, T.; Kaihatsu, Y.; Iskandar, F.; Wang, W.-N.; Okuyama, K. Facile Synthesis of New Full Color-Emitting BCNO Phosphors with High Quantum Efficiency. *Adv. Mater.* **2008**, *20*, 3235–3238.

[11] Liu, X.; Ye, S.; Qiao, Y.; Dong, G.; Zhanga, Q.; Qiu, J. Facile synthetic strategy for efficient and multi-color fluorescent BCNO nanocrystals. *Chem. Commun.* **2009**, 4073–4075.

[12] Lei, W.; Portehault, D.; Dimova, R.; Antonietti, M. Boron Carbon Nitride Nanostructures from Salt Melts: Tunable Water-Soluble Phosphors. *J. Am. Chem. Soc.* **2011**, *133*, 7121–7127.

[13] Weng, Q.; Wang, X.; Zhi, C.; Bando, Y.; Golberg, D. Boron Nitride Porous Microbelts for Hydrogen Storage. *ACS Nano* **2013**, *7*, 1558–1565.

[14] Thomas, J.; Weston, N. E.; O'Connor, T. E. Turbostratic Boron Nitride, Thermal Transformation to Ordered-layer-lattice Boron Nitride. *J. Am. Chem. Soc.*, **1962**, *84*, 4619–4622.

[15] See, for instance: (a) Patiño, J.; López-Salas, N.; Gutiérrez, M. C.; Carriazo, D.; Ferrer, M. L.; del Monte, F. "Phosphorus-Doped Carbon-Carbon Nanotube Hierarchical Monoliths as True Three-Dimensional Electrodes in Supercapacitor Cells", *J. Mater. Chem. A*, **2016**, *4*, 1251–1263. (b) Wang, J.; Zhang, X. Binary Crystallized Supramolecular Aerogels Derived from Host-Guest Inclusion Complexes. *ACS Nano* **2015**, *9*, 11389–11397.

[16] For some recent reviews, see: (a) Nardecchia, S.; Carriazo, D.; Ferrer, M. L.; Gutiérrez, M. C.; del Monte, F. Three dimensional macroporous architectures and aerogels built of carbon nanotubes and/or graphene: synthesis and applications. *Chem. Soc. Rev.* **2013**, *42*, 794–830, (b) Kumar, N.; Subrahmanyam, K. S.; Chaturbedy, P.; Raidongia, K.; Govindaraj, A.; Hembram, K. P. S. S.; Mishra, A. K.;

Waghmare, U. V.; Rao, C. N. R. Three-dimensional macro-structures of two-dimensional nanomaterials. *Chem. Soc. Rev.* **2016**, *45*, 5541–5588.

[17] Among others: (a) Pettes, M. T.; Ji, H.; Ruoff, R. S.; Shi, L. Thermal Transport in Three-Dimensional Foam Architectures of Few-Layer Graphene and Ultrathin Graphite. *Nano Lett.* **2012**, *12*, 2959−2964, (b) Chen, Z.; Xu, C.; Ma, C.; Ren, W.; Cheng, H.-M. Lightweight and flexible graphene foam composites for high-performance electromagnetic interference shielding. *Adv. Mater.* **2013**, *25*, 1296−1300.

[18] Among others: (a) Loeblein, M.; Tay, R. Y.; Tsang, S. H.; Ng, W. B.; Teo, E. H. T. Configurable three-dimensional boron nitride-carbon architecture and its tunable electronic behavior with stable thermal performances. *Small* **2014**, *10*, 2992−2999, (b) Loeblein, M.; Bolker, A.; Tsang, S. H.; Atar, N.; Uzan-Saguy, C.; Verker, R.; Gouzman, I.; Grossman, E.; Teo, E. H. T. 3D Graphene-Infused Polyimide with Enhanced Electrothermal Performance for Long-Term Flexible Space Applications. *Small* **2015**, *11*, 6425−6434, (c) Rousseas, M.; Goldstein, A. P.; Mickelson, W.; Worsley, M. A.; Woo, L.; Zettl, A. Synthesis of Highly Crystalline sp^2-Bonded Boron Nitride Aerogels. *ACS Nano* **2013**, *7*, 8540−8546, (d) Li, T.; Wang, L.; Zhang, K.; Xu, Y.; Long, X.; Gao, S.; Li, R.; Yao, Y. Freestanding Boron Nitride Nanosheet Films for Ultrafast Oil/Water Separation. *Small* **2016**, *12*, 4960−4965, (e) Song, Y.; Li, B.; Yang, S.; Ding, G.; Zhang, C.; Xie, X. Ultralight boron nitride aerogels via template-assisted chemical vapor deposition. *Sci. Reports* **2015**, *5*, Article number: 10337, (f) Harley-Trochimczyk, A.; Pham, T.; Chang, J.; Chen, E.; Worsley, M. A.; Zettl, A.; Mickelson, W.; Maboudian R. Platinum Nanoparticle Loading of Boron Nitride Aerogel and Its Use as a Novel Material for Low-Power Catalytic Gas Sensing. *Adv. Funct. Mater.* **2016**, *26*, 433−439.

[19] Among others: (a) Lei, W.; Mochalin, V. N.; Liu, D.; Qin, S.; Gogotsi, Y.; Chen, Y. Boron nitride colloidal solutions, ultralight aerogels and freestanding membranes through one-step exfoliation and functionalization *Nat. Commun.* **2015**, *6*, Article number: 8849, (b) Zeng, X.; Ye, L.; Yu, S.; Sun, R.; Xu, J.; Wong, C.-P. Facile Preparation of Superelastic and Ultralow Dielectric Boron Nitride Nanosheet Aerogels via Freeze-Casting Process. *Chem. Mater.* **2015**, *27*, 5849–5855.

[20] Jun, Y.-S.; Lee, E. Z.; Wang, X.; Hong, W. H.; Stucky, G. D.; Thomas, A. From Melamine-Cyanuric Acid Supramolecular Aggregates to Carbon Nitride Hollow Spheres. *Adv. Funct. Mater.* **2013**, *23*, 3661−3667.

[21] Peer, M.; Lusardi, M.; Jensen, K. F. Facile Soft-Templated Synthesis of High-Surface Area and Highly Porous Carbon Nitrides. *Chem. Mater.*, **2017**, *29*, 1496–1506.

[22] Xu, W.; Dong, M.; Gersen H.; Rauls, E.; Vázquez-Campos, S.; Crego-Calama, M.; Reinhoudt, D. N.; Stensgaard, I.; Laegsgaard, E.; Linderoth, T. R.; Besenbacher, F. Cyanuric Acid and Melamine on Au (111): Structure and Energetics of Hydrogen-Bonded Networks. *Small* **2007**, *3*, 854−858.

[23] Roy, B.; Bairi, P.; Saha, A.; Nandi, A. K. Variation of physical and mechanical properties in the bicomponent hydrogels of melamine with positional isomers of hydroxybenzoic acid *Soft Matter* **2011**, *7*, 8067−8076.

[24] Saha, A.; Roy, B.; Garai, A.; Nandi, A. K. Two-Component Thermoreversible Hydrogels of Melamine and Gallic Acid. *Langmuir* **2009**, *25*, 8457−8461.

[25] Czepirski, L.; Jagiello, J. Virial-type thermal equation of gas-solid adsorption, *Chem. Eng. Sci.*, **1989**, *44*, 797–801.

[26] Kawasaki, T.; Kuroda, Y.; Nishikawa, H. The crystal structure of melamine diborate. *J. Ceram. Soc. Jpn.* **1996**, *104*, 935–938.

[27] Panicker, C. Y.; Varghese, H. T.; John, A.; Philip, D.; Nogueira, H. I. S. Vibrational spectra of melamine diborate, $C_3N_6H_6{\cdot}2H_3BO_3$. *Spectrochim. Acta A* **2002**, *58*, 1545–1551.

[28] Roy, A.; Choudhurya, A.; Rao, C. N. R. Supramolecular hydrogen-bonded structure of a 1:2 adduct of melamine with boric acid. *J. Molec. Struct.* **2002**, *613*, 61–66.

[29] Ma, R.; Bando, Y.; Sato, T.; Kurashima, K. Growth, Morphology, and Structure of Boron Nitride Nanotubes, *Chem. Mater.* **2001**, *13*, 2965−2971

[30] Zhang, X.; Lu, Z.; Lin, J.; Li, L.; Fan, Y.; Hu, L.; Xu, X.; Meng, F.; Zhao, J.; Tang, C. Luminescence properties of BCNO phosphor prepared by a green and simple method, *Mater. Lett.* **2013**, *194*, 72–75

[31] Estroff, L. A.; Hamilton, A. D. Water Gelation by Small Organic Molecules, *Chem. Rev.* **2004**, *104*, 1201–1217

[32] Zhang, S.; Dokko, K.; Watanabe, M. Carbon materialization of ionic liquids: from solvents to materials, *Mater. Horiz.* **2015**, *2*, 168-197

[33] Chatterjee, S.; Saito, T. Lignin-Derived Advanced Carbon Materials, *ChemSusChem* **2015**, *8*, 3941–3958

[34] Yang, Y.; Le, T.; Kang, F.; Inagaki, M. Polymer blend techniques for designing carbon materials, *Carbon* **2017**, *111*, 546–568

[35] You, B.; Yin, P.; Zhang, J.; He, D.; Chen, G.; Kang, F.; Wang, H.; Deng, Z.; Li, Y. Hydrogel-derived non-precious electrocatalysts for efficient oxygen reduction, *Sci. Reports* **2015**, *5*, Article number: 11739

[36] Zhang, S.; Gao, L.; Fan, D.; Lv, X.; Li, Y.; Yan, Z. Synthesis of boron-doped g-C3N4 with enhanced electro-catalytic activity and stability. *Chem. Phys. Lett.* **2017**, *672*, 26–30

[37] Zhang, X.; Jia, X.; Liu, H.; Lu, Z.; Ma, X.; Meng, F.; Zhao, J.; Tang, C. Spectral properties and luminescence mechanism of red emitting BCNO phosphors. *RSC Adv.* **2015**, *5*, 40864–40871

[38] Fellinger, T.-P.; Su, D. S.; Engenhorst, M.; Gautam, D.; Schlögl, R.; Antonietti, M. Thermolytic synthesis of graphitic boron carbon nitride from an ionic liquid precursor: mechanism, structure analysis and electronic properties. *J. Mater. Chem.* **2012**, *22*, 23996–24005

[39] Suryamas, A. B.; Munir, M. M.; Ogi, T.; Khairurrijal; Okuyama, K. Intense green and yellow emissions from electrospun BCNO phosphor nanofibers. *J. Mater. Chem.* **2011**, *21*, 12629–12631

[40] Ristein, J.; Stief, R. T.; Ley, L.; Beyer, W. A comparative analysis of a-C:H by infrared spectroscopy and mass selected thermal effusion. *J. Appl. Phys.* **1998**, *84*, 3836–3847

[41] Casiraghi, C.; Piazza, F.; Ferraria, A. C.; Grambole, D.; Robertson, J. Bonding in hydrogenated diamond-like carbon by Raman spectroscopy. *Diamond & Related Materials* **2005**, *14*, 1098–1102

[42] Ozturk, B.; de-Luna-Bugallo, A.; Panaitescu, E.; Chiaramonti, A. N.; Liu, F.; Vargas, A.; *et al.*, Atomically thin layers of B–N–C–O with tunable composition. *Sci. Adv.* **2015**, *1*, e1500094

[43] Jayaramulu, K.; Kumar, N.; Hazra, A.; Maji, T. K.; Rao, C. N. R. A Nanoporous Borocarbonitride (BC4N) with Novel Properties Derived from a Boron-Imidazolate-Based Metal–Organic Framework. *Chem. Eur. J.* **2013**, *19*, 6966–6970

[44] Kumar, R.; Gopalakrishnan, K.; Ahmad, I.; Rao, C. N. R. BN–Graphene Composites Generated by Covalent Cross-Linking with Organic Linkers. *Adv. Funct. Mater.* **2015**, *25*, 5910–5917

[45] Dwivedi, J.; Kumar, P.; Kedawat, G.; Gupta, B. K. New emerging rare-earth free yellow emitting 2D BCNO nanophosphor for white light emitting diodes. *New J. Chem.* **2015**, *39*, 5161–5170

[46] Gutiérrez, M. C.; Picó, F.; Rubio, F.; Amarilla, J. M.; Palomares, F. J.; Ferrer, M. L. *et al.*, PPO15-PEO22-PPO15 block copolymer assisted synthesis of monolithic macro- and microporous carbon aerogels exhibiting high conductivity and remarkable capacitance. *J. Mater. Chem.* **2009**, *19*, 1236–1240

[47] Leung, T. Y.; Man, W. F.; Lim, P. K.; Chan, W. C.; Gaspari, F.; Zukotynski, S. Determination of the sp3/sp2 ratio of a-C:H by XPS and XAES. *J. Non-Crystal. Solids* **1999**, *254*, 156–160

[48] Bae, Y.-S.; Mulfort, K. L.; Frost, H.; Ryan, P.; Punnathanam, S.; Broadbelt, L. J.; *et al.*, Separation of CO2 from CH4 Using Mixed-Ligand Metal-Organic Frameworks. *Langmuir* **2008**, *24*, 8592–8598

[49] Liu, L.; Yang, J.; Li, J.; Dong, J.; Sisak, D.; Luzzatto, M.; McCusker, L. B. Ionothermal Synthesis and Structure Analysis of an Open-Framework Zirconium Phosphate with a High CO2/CH4 Adsorption Ratio. *Angew. Chem. Int. Ed.* **2011**, *50***,** 8139–8142.

[50] Dybtsev, C. N.; Chun, H.; Yoon, S. H.; Kim, D.; Kim, K. Microporous Manganese Formate: A Simple Metal-Organic Porous Material with High Framework Stability and Highly Selective Gas Sorption Properties, *J. Am. Chem. Soc.*, **2004**, *126*, 32–33.

[51] Jeon, Y.-M.; Armatas, G. S.; Heo, J.; Kanatzidis, M. G.; Mirkin, C. A. Amorphous Infinite Coordination Polymer Microparticles: A New Class of Selective Hydrogen Storage Materials, *Adv. Mater.*, **2008**, *20*, 2105–2110.

[52] Katsoulidis, A. P.; Kanatzidis, M. G. Phloroglucinol Based Microporous Polymeric Organic Frameworks with –OH Functional Groups and High CO2 Capture Capacity, *Chem. Mater.*, **2011**, *23*, 1818–1824.

[53] López-Salas, N.; Gutiérrez, M. C.; Ania, C. O.; Fierro, J. L. G.; Ferrer, M. L.; del Monte, F., Efficient nitrogen-doping and structural control of hierarchical carbons using unconventional precursors in the form of deep eutectic solvents. *J. Mater. Chem. A*, **2014**, *2*, 17387–17399

[54] Patiño, J.; Gutiérrez, M. C.; Carriazo, D.; Ania, C. O.; Fierro, J. L. G.; Ferrer, M. L.; del Monte, F. DES assisted synthesis of hierarchical nitrogen doped carbon molecular sieves for selective CO2 versus N2 adsorption, *J. Mater. Chem. A*, **2014**, *2*, 8719–8729

[55] Patiño, J.; Gutiérrez, M. C.; Carriazo, D.; Ania, C. O.; Parra, J. B.; Ferrer, M. L.; del Monte, F. Deep eutectic assisted synthesis of carbon adsorbents highly suitable for low-pressure separation of CO_2–CH_4 gas mixtures, *Energy Environ. Sci.*, **2012**, *5*, 8699–8707.

[56] Garrido, J.; Linares-Solano, A.; Martín-Martínez, J. M.; Molina-Sabio, M.; Rodriguez-Reinoso, F.; Torregrosa, R. Use of N2 vs. C02 in the Characterization of Activated Carbons, *Langmuir*, **1987**, *3*, 76–81.

[57] Patiño, J.; Gutiérrez, M. C.; Carriazo, D.; Ania, C. O.; Parra, J. B.; Ferrer, M. L.; del Monte, F. Deep eutectic assisted synthesis of carbon adsorbents highly suitable for low-pressure separation of CO_2–CH_4 gas mixtures, *Energy Environ. Sci.*, **2012**, *5*, 8699–8707.

[58] Zhao Y.; Zhao, L.; Yao, K. X.; Yang, Y.; Zhang, Q.; Han, Y. Novel porous carbon materials with ultrahigh nitrogen contents for selective CO_2 capture. *J. Mater. Chem.* **2012**, *22*, 19726–19731.

[59] Fan, X.; Zhang, L.; Zhang, G.; Shu, Z.; Shi, J. Chitosan derived nitrogen-doped microporous carbons for high performance CO_2 capture. *Carbon* **2013**, *61***,** 423–430.

[60] Llewellyn, P. L.; Bourrelly, S.; Serre, C.; Vimont, A.; Daturi, M.; Hamon, L.; *et al.*, High Uptakes of CO_2 and CH_4 in Mesoporous Metal—Organic Frameworks MIL-100 and MIL-101, *Langmuir*, **2008**, *24*, 7245–7250.

[61] Ashourirad, B.; Sekizkardes, A. K.; Altarawneh, S.; El-Kaderi, H. M. Exceptional Gas Adsorption Properties by Nitrogen-Doped Porous Carbons Derived from Benzimidazole-Linked Polymers, *Chem. Mater.*, **2015**, *27*, 1349–1358

[62] Nugent, P.; Belmabkhout, Y.; Burd, S. D.; Cairns, A. J.; Luebke, R.; Forrest, K.; Pham, T.; Ma, S.; Space, B.; Wojtas, L.; Eddaoudi, M.; Zaworotko, M. J. Porous materials with optimal adsorption thermodynamics and kinetics for CO2 separation. *Nature* **2013**, *495***,** 80–84.

[63] Chang, G.; Shang, Z.; Yu, T.; Yang, L. Rational design of a novel indole-based microporous organic polymer: enhanced carbon dioxide uptake via local dipole–πinteractions. *J. Mater. Chem. A* **2016**, *4*, 2517–2523.

[64] Banerjee, R.; Furukawa, H.; Britt, D.; Knobler, C.; O'Keeffe, M.; Yaghi, O. Control of Pore Size and Functionality in Isoreticular Zeolitic Imidazolate Frameworks and their Carbon Dioxide Selective Capture Properties, *J. Am. Chem. Soc.*, **2009**, *131*, 3875–3877.

[65] Huang, K.; Liu, F.; Dai, S. Solvothermal synthesis of hierarchically nanoporous organic polymers with tunable nitrogen functionality for highly selective capture of CO_2. *J. Mater. Chem. A* **2016**, *4*, 13063–13070.

[66] Espinal, L.; Wong-Ng, W.; Kaduk, J. A.; Allen, A. J.; Snyder, C. R.; Chiu, C.; *et al.*, Time-dependent CO_2 sorption hysteresis in a one-dimensional microporous octahedral molecular sieve. *J. Am. Chem. Soc.* **2012**, *134*, 7944−7951.

[67] Liu, F.; Huang, K.; Wu, Q.; Dai, S. Solvent-free self-assembly to the synthesis of nitrogen-doped ordered mesoporous polymers for highly selective capture and conversion of CO_2. *Adv. Mater.* 2017, *29*, DOI: 10.1002/adma.201700445.

[68] Sun, L.-B.; Li, A.-G.; Liu, X.-D.; Liu, X.-Q.; Feng, D.; Lu, W.; *et al.*, Facile fabrication of cost-effective porous polymer networks for highly selective CO_2 capture. *J. Mater. Chem. A* **2015**, *3*, 3252–3256.

[69] Huang, K.; Liu, F.; Dai, S. Ionothermal synthesis and structure analysis of an open-framework zirconium phosphate with a high CO_2/CH_4 adsorption ratio. *Angew. Chem. Int. Ed.* **2011**, *50*, 8139–8142.

[70] For a recent review describing numerous examples, see: D'Alessandro, D. M.; Smit, B.; Long, J. R. Carbon dioxide capture: prospects for new materials. *Angew. Chem. Int. Ed.* **2010**, *49*, 6058–6082.

[71] Jagiello, J.; Bandosz, T. J.; Putyera K.; Schwarz, J. A. Adsorption near ambient temperatures of methane, carbon tetrafluoride, and sulfur hexafluoride on commercial activated carbons, *J. Chem. Eng. Data*, **1995**, *40*, 1288–1292.

[72] Sircar, S.; Golden, T. C.; Rao, M. B. Activated carbon for gas separation and storage, *Carbon*, **1996**, *34*, 1–12.

[73] Chen, H.; Yu, H.; Tang, Y.; Pan, M.; Yang, G.; Peng, F.; Wang, H.; Yang, J. Adsorption separation of carbon dioxide, methane, and nitrogen on Hb and Na-exchanged b-zeolite, *J. Nat. Gas Chem.*, **2008**, *17*, 391–396.

[74] Liu, L.; Yang, J.; Li, J.; Dong, J.; Sisak, D.; Luzzatto, M.; *et al.*, Ionothermal synthesis and structure analysis of an open-framework Zirconium phosphate with a high CO_2/CH_4 adsorption ratio. *Angew. Chem. Int. Ed.* **2011**, *50*, 8139–8142.

[75] Rabbani, M. G.; El-Kaderi, H. M. Synthesis and Characterization of Porous Benzimidazole-Linked Polymers and Their Performance in Small Gas Storage and Selective Uptake, *Chem. Mater.*, **2012**, *24*, 1511–1517

[76] Klumpen, C.; Breunig, M.; Homburg, T.; Stock, N.; Senker, J. Microporous organic polyimides for CO_2 and H_2O capture and separation from CH_4 and N_2 mixtures: interplay between porosity and chemical function. *Chem. Mater.* 2016, *28*, 5461–5470.

[77] Lourenço, M. A. O. et al. Interaction of CO_2 and CH_4 with functionalized periodic mesoporous phenylene−silica: periodic DFT calculations and gas adsorption measurements. *J. Phys. Chem. C* **120,** 3863−3875 (2016).